Modality of odor perception is transmitted to cortical brain regions from the olfactory bulb

Michelle F. Craft[1], Andrea K. Barreiro[2], Shree Hari Gautam[3], Woodrow L. Shew[3], Cheng Ly[1,*]

1 Department of Statistical Sciences and Operations Research, Virginia Commonwealth University, Richmond, Virginia, United States
2 Department of Mathematics, Southern Methodist University, Dallas, Texas, United States
3 Department of Physics, University of Arkansas, Fayetteville, Arkansas, United States

∗cly@vcu.edu

Abstract

Odor perception is the impetus for important animal behaviors, most obviously for feeding but also for mating and communication. There are two predominate modes of odor processing: odors pass through the front of the nose (orthonasal) while inhaling and sniffing, or through the rear (retronasal) during exhalation and while eating. Despite the importance of olfaction for an animal's well-being and specifically that ortho and retro naturally occur, it is unknown how the modality (ortho versus retro) is even transmitted to cortical brain regions, which could significantly affect how odors are processed and perceived. We show mitral cell neurons in the rat olfactory bulb reliably transmit ortho versus retro food odor stimuli. Drug manipulations affecting $GABA_A$ that control synaptic inhibition lead to worse decoding of ortho/retro, independent of whether overall inhibition increases or decreases, suggesting that the olfactory bulb circuit is naturally structured to encode this important aspect of odors. Detailed data analysis paired with a firing rate model to capture population trends in spiking statistics shows how this circuit with baseline inhibition can encode odor modality. We have not only shown that ortho versus retro information is encoded to downstream brain regions, but models and analyses reveal the network dynamics that promotes this encoding.

Author summary

Olfaction is instrumental in a variety of animal behaviors, and has two predominate modes of odor delivery, naturally passing through the front of nose (orthonasal) while inhaling and sniffing, or through the rear (retronasal) during exhalation and while eating. Yet it is unknown how the mode of olfaction (ortho or retro) is even encoded to olfactory cortical brain areas. We show here that the spiking activity of neurons in the olfactory bulb reliably transmits this information to cortical brain regions. Furthermore, drug manipulations that either strengthen or weaken inhibition degrades ortho/retro information, suggesting that the olfactory bulb circuit is naturally structured to well-encode this important aspect of odor input. Using computational models and theory, we analyze how the neural network attributes lead to encoding of ortho/retro input. We show that higher brain regions have access to information about the mode of processing and detail how this can occur, which should have significant implications for how odors are perceived since retro odors occur during feeding.

Introduction

Olfaction is driven by odor molecules entering the nasal cavity that induce a cascade of action potentials in the nervous system to transmit and process odor information. There are two routes by which odor molecules can enter the nasal cavity: through the nostrils during inhalation and sniffing (**ortho**), or from the throat during exhalation and while eating (**retro**). Orthonasal stimulation is by far the most commonly studied modality despite retronasal naturally occurring during eating. Prior imaging studies have shown differences in the activation of the regions of the nasal epithelium with ortho and retro stimulation [1–3], and Small et al [4] shows that ortho/retro information is transmitted to cortical brain regions in humans but does not detail the mechanisms for this. Thus, how ortho/retro information is transmitted to cortical brain regions is unknown; also, what are the network attributes that promote efficient encoding of ortho versus retro input?

These questions are important for several reasons. Humans are able to discriminate whether food odors are delivered ortho or retronasally without being told which modality [5] but it is unknown whether this information is propagated from the 'bottom up' or if detection is solely from higher brain regions. Imaging studies have shown that at least with food odors, ortho versus retro are two distinct modalities, rather than 2 different routes to the same modality, independent of odor intensity [6]. Moreover, there is evidence that cortical processing depends on ortho versus retro [7], and humans report perceiving smells differently depending on ortho/retro modality [4,8].

Before odor information reaches the brain, it is processed in the olfactory bulb (**OB**) and relayed to higher brain regions via excitatory mitral cells (**MC**s) (and tufted cells). Thus, the OB is critical for determining whether ortho versus retronasal odors are encoded before being conveyed to the brain for processing and perception. More broadly, OB activity is tied to odor perception [9]. While the role of inhibitory cells in influencing the OB processing of ortho versus retro odors is as yet unknown, inhibition has been shown to play a key role in many other aspects of OB processing. OB inhibition is known to alter activity patterns that represent odors [10], granule cells that provide inhibition reflect changes in odor concentration [11], and OB inhibition levels alter odor discrimination dynamics [12]. Thus motivating our experiments consisting of *in vivo* rat recordings of MCs in the OB with both decreased and increased levels of $GABA_A$ synaptic inhibition via drug manipulations. The rats were anesthetized and a double tracheotomy was performed allows the breathing air flow to bypass the nasal cavity, thus allowing precise control of ortho versus retro stimulation.

We show that the mode of the input stimuli (ortho versus retro) is indeed transmitted to cortical brain regions. We find the encoding is generally good and well above chance level for the intact circuit and even with altered levels of inhibition. Thus downstream brain regions readily have access to ortho versus retronasal odor modality with spiking activity from the OB. Importantly, the altered circuits with both increases (via **Mus**cimol application, a $GABA_A$ agonist) and decreases in inhibition (via **Bic**uculline, a $GABA_A$ antagonist) leads to overall worse encoding. This suggests that the intact OB circuit is optimal for encoding ortho versus retro modality.

Our rich data enables investigation of the OB circuit mechanisms that promote this encoding with a computational model. We show how a simple excitatory-inhibitory (**E-I**) reciprocally coupled pair captures the modality dependent differences in population firing rate. We model trial-to-trial spike rate variability to be largely consistent with our data and so that the model can encode orth-/retro-like stimuli. We find that modality encoding is degraded when inhibition is either increased or decreased, as observed in our data. Given the commonality of reciprocally coupled excitatory-inhibitory circuits, these results may apply outside of the OB, specifically to where stimuli have temporal differences.

Results

We collected spike data with multi-electrode array recordings of urethane anesthetized rats in the OB mitral cell layer, where each cell (MC) was subject to the same odor delivered with ortho and retro stimulation (Fig 1Ai), repeated for 10 trials for each modality. In addition, two drugs were applied to alter the circuit: a $GABA_A$ antagonist (**Bic**uculline) and a $GABA_A$ agonist (**Mus**cimol). See Table 1 for details of data collected. For reference, Fig 1Aii shows the population-averaged firing rate (first get trial-average firing rate for each MC, then average over all MCs) by modality for a given drug preparation, with $t = 0$ denoting time of odor presentation that is held for 1 s. This is commonly referred to as the peri-stimulus time histogram (**PSTH**).

Table 1. Number of rats and respective individual cells for each drug preparation subject to the food odor Ethyl Butyrate (EB).

	No Drug	Bicuculline	Muscimol
Rats	8	4	3
Cells	913	413	419

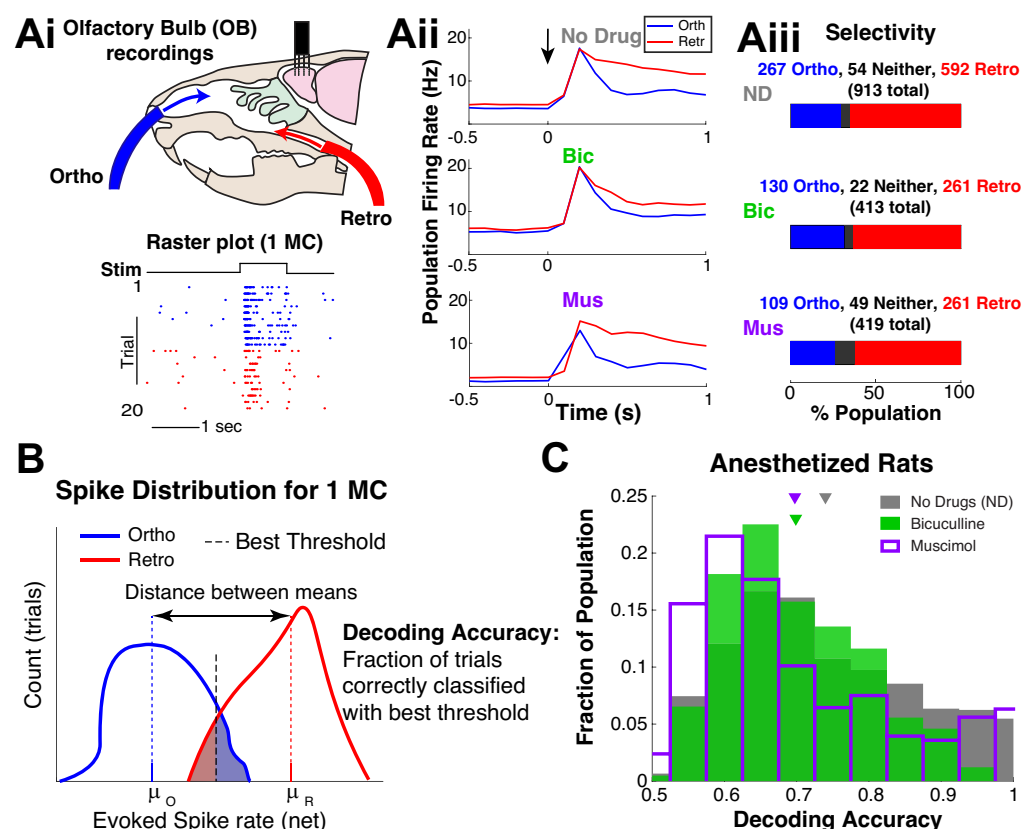## Individual MCs encode ortho versus retro

To remain agnostic to how higher brain regions decode population activity, we predominately consider individual MCs encoding of odor modality. Individual MC coding is also a logical first step [13]. We use net spiking rate to account for large variation of spontaneous spiking within individual trials [14] and to account for state changes, i.e., drug preparations result in significant changes in spontaneous spiking (Fig 2B). Specifically, the net spiking rate $\vec{x}_k$ for the kth trial, $k = 1, 2, ..., N$, is the sum of the evoked spike counts (normalized by time window $T_{ev} = 0.9$ s) minus the spikes in the spontaneous state (normalized by time window $T_{sp} = 2$ s):

$$\vec{x}_k = \frac{1}{T_{ev}} \Big(\# \text{ Evoked spikes in } T_{ev} \Big) - \frac{1}{T_{sp}} \Big(\# \text{ Spontaneous spikes in } T_{sp} \Big) \quad (1)$$

(see Eq (4) in **Materials and methods**). The time windows were systematically chosen from a range of possible values, see **S1 Fig** and **Materials and methods** for details. To assess whether MCs might prefer one modality over the other, we compare the trial-averaged net spiking rate for ortho and retro as a measure of selectivity (Fig 1Aiii, a tuning 'curve' with 2 points). Most MCs 'prefer' or spike more with retro than ortho ($\approx 63\%$), and the proportions do not vary much as drug preparations change.

We define decoding accuracy as the fraction of trials correctly classified by a threshold that maximizes decoding accuracy, so this is a measure of information accessible by an ideal observer from each MC individually (Fig 1B). We only consider Ethyl Butyrate (**EB**), a common food odor, because only food odors are perceived retronasally [4]. Moreover, numerous studies have shown that non-food odors delivered retronasally degrade human perception of odors [5, 6, 8].

The OB circuit is naturally structured to well-encode ortho versus retro. Figure 1C shows the spiking activity of individual MCs encode (measured by decoding accuracy) ortho versus retro for the vast majority of cells. There is a wide range of decoding accuracies varying between 0.5 (i.e., chance) and 1 (i.e., perfect decoding), with no drug the mean decoding accuracy is 0.74, and both Mus and Bic have **lower** average decoding accuracies of 0.69 for both. Further, the differences in the mean decoding accuracy are all statistically significant ($\alpha = 0.01$) using three tests: two-sample $t-$test ($p_{ND,Bic} = 2.2 \times 10^{-10}, p_{ND,Mus} = 1.6 \times 10^{-7}$), Wilcoxon rank sum test

Fig 1. Individual mitral cells encode olfaction mode. Ai) Experiment setup to test whether OB MCs encode ortho versus retro stimulation, with example raster plot for 1 MC. **Aii)** Population-averaged firing rate (trial-avg for each MC then population-averaged), i.e., **PSTH** for each modality and drug preparation; $t = 0$ denotes when Ethyl Butyrate (food odor) is presented. **Aiii)** The proportion of population that are ortho (or retro) selective, i.e., ortho selective $\Leftrightarrow$ higher trial averaged (net) firing rate for ortho than retro. **B)** Schematic of how decoding accuracies are calculated for each MC: using net spike rate. **C)** Distribution of decoding accuracies of MC with 3 different preparations: intact no drug (gray), less inhibition via Bic (green) and more inhibition via Mus (purple). Mean decoding accuracy for no drug is 0.74, with Bic and Mus the means are: 0.69; these differences are all statistically significant ($\alpha = 0.01$ with two-sample $t-$test assuming unequal var, Wilcoxon rank sum test, and one-way ANOVA). Net spikes in a given trial is the number of evoked spikes (0.9 s window) minus spontaneous spikes (2 s window). Windows were determine systematically to maximize decoding accuracy $p-$values, see **S1 Fig** and **Materials and methods**.

$(p_{ND,Bic} = 1.2 \times 10^{-6}, p_{ND,Mus} = 1.5 \times 10^{-10})$, and one-way ANOVA $\qquad$ 92
$(p_{ND,Bic} = 9.2 \times 10^{-9}, p_{ND,Mus} = 6.4 \times 10^{-8})$. See Table 2 for these $p-$values. $\qquad$ 93

Table 2. Population Decoding Accuracy: significance ($p-$values) of average (over MC) decoding accuracies shown in Figure 1C. Using 3 tests: two-sample $t-$test assuming unequal variance, Wilcoxon rank sum test, and one-way ANOVA.

Relationship	$t-$test	Rank Sum	ANOVA
Bic $<$ ND	2.2×10^{-10}	1.2×10^{-6}	9.2×10^{-9}
Mus $<$ ND	1.6×10^{-7}	1.5×10^{-10}	6.4×10^{-8}

Drug effects on mean population activity

To better understand the dynamics of MC decoding accuracy, we consider how $GABA_A$ (ant-)agonists effect population activity. Although population activity is a simple and coarse measure that neglects individual cell heterogeneity, it still can be insightful for determining average or expected trends. A characteristic of an individual MC that might be indicative of encoding fidelity is the distance between the trial-averaged (net) spike rate of ortho and retro stimulation $|\mu_R - \mu_O|$ (Fig 1B). We expect larger distances to coincide with better decoding accuracy than smaller distances, if all other factors are equal. Fig 2A shows very strong correlations (Pearson's and Spearman's rank) between $|\mu_R - \mu_O|$ and decoding accuracies for all drug preparations, although other factors affect decoding accuracy (e.g., trial-to-trial variance) since there is dispersion for a given decoding accuracy value. Nevertheless, this motivates considering the population-averaged spiking activity as a means to better understand the dynamics of decoding accuracy.
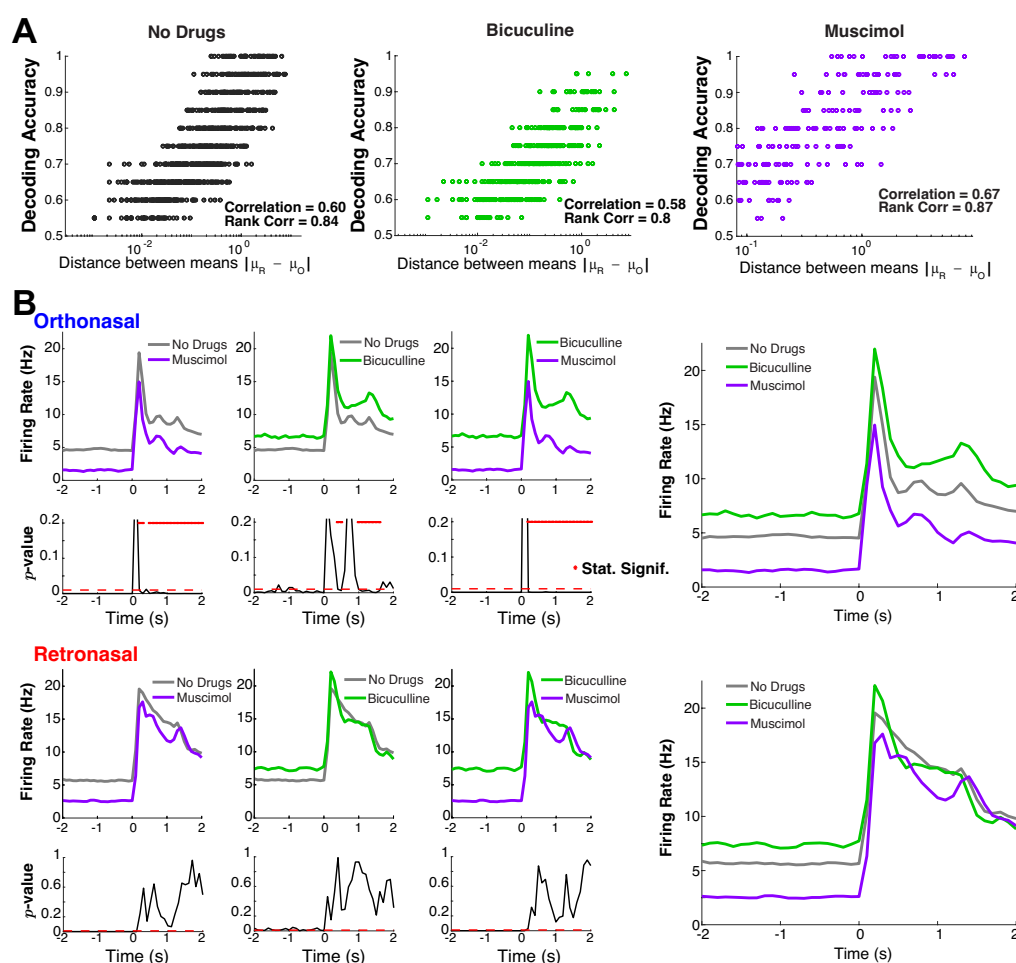
Fig 2. Retronasal response is more robust to changes in OB inhibition.
A) Distance between trial-averaged mean $|\mu_R - \mu_O|$ is strongly correlated with decoding accuracy. **B**) Drug effects on evoked population PSTH are different with statistically significant effects only with ortho stimulation (not retro). The $p-$values are from two-sample $t-$test assuming unequal variances.

The affects of the $GABA_A$ (ant-)agonists on population firing rate depend on the odor modality; only ortho evoked firing rates show statistically significant differences in the mean (over MC population) PSTH. In comparing the population firing rates for a given modality (ortho or retro), rather than comparing ortho versus retro for a given drug preparation (Fig 1Aii), we find some stark differences (Fig 2B). As expected, Mus (increased inhibition) causes firing rates to decrease and Bic (less inhibition) causes firing rates to increase compared to no drug, especially in the spontaneous state. However, the evoked firing rates are **only** significantly different ($\alpha = 0.01$) with ortho stimulation, and **not** significantly different with retro stimulation. This holds for nearly all time points (see * in $p-$value plots of two sample $t-$test with unequal variance). This effect is clear in the right-most column of Fig 2B.

If we assume these population trends (Fig 2B) hold individually for MCs (drugs only effect spiking rate with ortho but not retro), then we might expect decoding accuracies to change in specific ways: if ortho spiking is less than retro with no drug, then Bic should increase spiking (shift histograms to the right) causing more overlap and lower decoding accuracy. For exposition purposes, these results are detailed in **S2 File** and **S3 Fig**.

Drug effects on trial-to-trial variability

In addition to the mean (net) spiking rate over trials, the trial-to-trial variability plays a key role in decoding accuracy differences. Here we consider the variance of spiking activity over trials for each MC and test whether the population average is different across drug preparations. We find with Mus application, the average trial variability is smallest, followed by Bic, then no drug (i.e., Mus < Bic < no drugs) – this trend holds for ortho and only somewhat for retro. The significance measured by $p-$values of this relationship are in Tables 3 and 4 for ortho and retro trials, respectively, using the same three statistical tests as before. For ortho stimulation, Mus < no drugs is significant for all three tests ($\alpha = 0.01$), while Bic < no drug and Mus < Bic are only significant with Wilcoxon rank sum test. For retro stimulation, again only the Wilcoxon rank sum test shows this relationship is significant (all with $\alpha = 0.01$ except for Bic < ND for retro where $p = 0.027$). Overall, the Bic < ND relationship is not as strong as the others, and the trend Mus < Bic < no drugs is stronger with ortho stimulation.

Table 3. Ortho stimulation only: significance ($p-$values) of average (over MC) trial variance differences between drugs with various statistical tests. Using same 3 tests as before; **ND**='no drug'.

Relationship	$t-$test	Rank Sum	ANOVA
Mus < ND	1.8×10^{-3}	9.0×10^{-8}	0.022
Mus < Bic	0.028	1.1×10^{-14}	0.027
Bic < ND	0.85	5.6×10^{-5}	0.86

Table 4. Retro stimulation only: significance ($p-$values) of average (over MC) trial variance differences between drugs with various statistical tests. Using same 3 tests as before; **ND**='no drug'.

Relationship	$t-$test	Rank Sum	ANOVA
Mus < ND	0.065	1.7×10^{-4}	0.145
Mus < Bic	0.42	2.6×10^{-7}	0.41
Bic < ND	0.43	0.027	0.48

Within all of the 3 drug preparations, the average trial variances for ortho versus

retro are statistically indistinguishable.

Model connects network dynamics and decoding accuracy

To reveal the neural network dynamics that explain our experimental data results, we use a firing rate model of the spiking activity. Our rich data set with 3 total drug preparations enables a model framework that is highly constrained by data [15–17]. In addition, we incorporate known differences in temporal dynamics of ORN inputs to MCs with ortho versus retro stimulation, supported by experiments [1–3, 18, 19]. Ortho stimulation results in fast increase and fast decrease of ORN inputs to MCs while retro input results in slower increase and slower decrease ORN inputs than ortho (Fig 3B). Although it is not definitive, Fig 2c of [3] suggests that the amplitude of ORN inputs with ortho are larger than retro (Fig 3B). We develop a principled model that is structurally the same with both odor modalities but will effectively have different dynamics stemming from different ORN inputs [20].

We first set out to implement an OB model that accounts for the large changes in population PSTH with GABA$_A$ (ant-)agonists with ortho stimulation only, and small (or no statistically significant) changes in population PSTH with retro ($\overline{\text{Fig 2B}}$). We use a reciprocally coupled 2 cell E-I network (Fig 3A), consistent with OB networks that have many such E-I pairs (granule cells and MCs, as well as periglomerular cells and MCs, are reciprocally connected with fast dendrodendritic synapses [21]). We do not distinguish between different GABA$_A$ inhibitory neurons so that the network dynamics are easier to understand, all of which is partially justified by our focus on individual MC decoding accuracy. We model the drug effects Bic (Mus) by decreasing (increasing) the coupling strength from I to E cell by 25% of the baseline value ($w_{EI} = 0.2$ with no drugs, arbitrary units, see Eqs (5)–(6) and Table 7).

We hypothesize that short-term plasticity could be a factor in explaining the differences of population firing between ortho/retro with GABA$_A$ (ant-)agonists because of known temporal differences in (ORN) inputs. There is indeed evidence of plasticity in the OB circuit [22, 23], specifically for short-term synaptic depression in the main OB [24] and from MC to granule cells [25]. Since the relative differences in firing rate with ortho are already large without plasticity (1st column in Table 5), honing in on decreasing the firing rate differences in retro (3rd column in Table 5) would make the model more consistent with the data (Fig 2B). We use short-term synaptic depression as a means to nonlinearly change the retro firing rates to diminish the differences because retro has longer lasting stimuli; we found that short-term facilitation made the model much less consistent with our data.

Table 5. Relative differences of firing rate model between no drug and inhibitory drugs in both modalities.
All percent differences are relative to no drug: $\left| \int_0^{T_{ev}} A_E^{\text{Drug}}(t)\, dt - \int_0^{T_{ev}} A_E^{\text{No Drug}}(t)\, dt \right| \Big/ \int_0^{T_{ev}} A_E^{\text{No Drug}}(t)\, dt$.

Relative Differences (%)	Ortho		Retro	
	Without Depression	With Depression	Without Depression	With Depression
No Drug / Bicuculline	61.14	51.46	20.97	8.88
No Drug / Muscimol	48.29	47.18	16.84	8.69

Figure 3C shows comparisons of various model outputs (Eqs (5)–(11)). The model indeed follows the firing rate modulation with GABA$_A$ (ant-)agonists with both odor modalities, and whether or not synaptic depression is included. Specifically, ortho MC firing rates (top left in Fig 3) with different drug preparations are well-separated, while the retro MC firing rates are pretty close together (bottom left in Fig 3). The effects of synaptic depression further narrows the differences in retro population PSTH among all 3 drug applications, while with ortho the differences across drug preps remain large (see
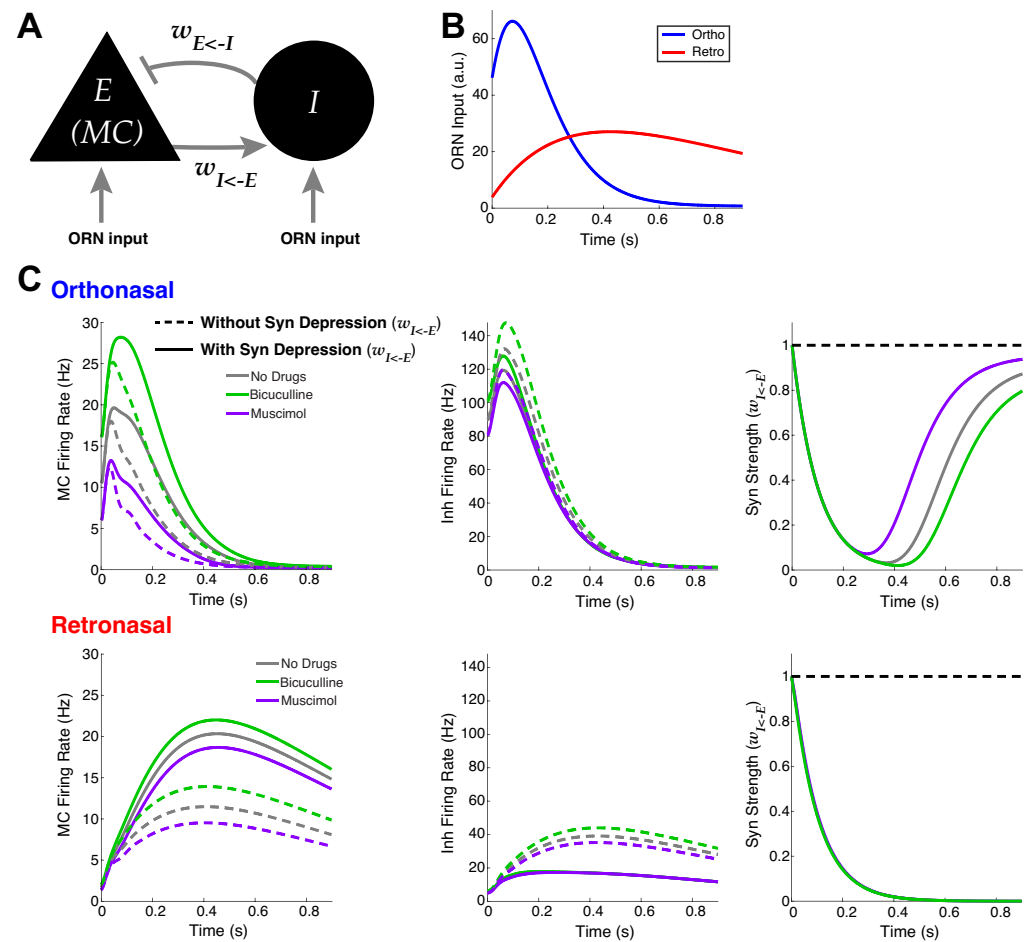
Fig 3. Firing rate model can capture effects of drugs, results are enhanced with synaptic depression. A) Schematic of reciprocally coupled E-I pair. **B)** Fixed ORN input profiles for ortho and retro based on experiments [1–3, 18, 19] (see main text). **C)** Wilson-Cowan firing rate model (Eqs (5)–(11)) output for ortho (top row) and retro (bottom row) stimulation, compared when synaptic depression is included (solid lines) or not included (dashed lines). Left column - E cell (MC) output, center column - I cell output, and right column - synaptic strengths (W_{IE}).

Table 5 for relative differences). Taken together, synaptic depression makes the model more inline with the data (Fig 2B). With retro stimuli and all 3 drug preparations, the E→I synaptic connections are depressed for longer so that the I-cell fires less, giving a boost to E-cell firing. In both modalities, there is overall higher E (MC) firing with short-term synaptic depression because of less inhibition (for all 3 drug preparations). Synaptic depression effectively diminishes the reciprocal loop so that the inhibitory drug effects are weakened.

With the neural dynamics captured in our model, we turn to connecting the model to decoding accuracy. The firing rate model does not explicitly have trial-to-trial variability, which is an important component to decoding accuracy of a given trial. Therefore, we next investigated decoding using a simple parametric model of trial variability, the negative binomial distribution. Specifically, for each drug (No Drug/Bic/Mus) and each input (ortho/retro), we fit a negative binomial distribution to the distribution of outcomes. The two distribution parameters were chosen so that: 1)

the mean of distribution coincided with the model spiking rate $\frac{1}{T_{ev}} \int_0^{T_{ev}} A_E(t)\, dt$ (solid curves in Fig 3C, left column), and 2) the decoding accuracy equaled the decoding accuracy observed in the experimental data.

The negative binomial distribution has distribution: $\frac{\Gamma(x+r)}{x!\Gamma(r)} \rho^r (1-\rho)^x$ with parameters: $\rho \in (0,1)$ and $r > 0$. We manually (by trial and error) determine the parameter ρ for each modality and drug preparation, which are all the same ρ except for retro with Mus (see Table 7), after which the r parameter is determined:

$$r = \frac{\rho}{1-\rho} \left(\frac{1}{T_{ev}} \int_0^{T_{ev}} A_E(t)\, dt \right) \tag{2}$$

since the mean of the negative binomial is $\frac{r(1-\rho)}{\rho}$. We chose ρ for each regime so that the resulting decoding accuracy would match the averages from the experiments: 0.74 (no drug), 0.69 (Bic and Mus).

The results are summarized in Fig 4A–C. We simulated 50,000 trials and found the optimal threshold to determine decoding accuracy.

To further validate our model, we test whether the specified parameter values for ρ robustly results in the no drug case generally has better decoding accuracy than Bic and Mus. We start with the base model of spiking rate: $\frac{1}{T_{ev}} \int_0^{T_{ev}} A_E(t)\, dt$ (solid curves in Fig 3C, left column) and perturb these values to get different means: $\mu^* = \frac{1}{T_{ev}} \int_0^{T_{ev}} A_E(t)\, dt \pm M_{O/R}$, where $M_O \in \{-2, \ldots, 4\}$ Hz on 25 equally spaced points and $M_R \in \{-6, \ldots, 9\}$ Hz on 31 equally spaced points. Once a mean is specified, we use the same p (Table 7) and set r^* to correspond to the mean μ^*:

$$r^* = \frac{\rho}{1-\rho} \mu^*, \tag{3}$$

and simulate 50,000 trials to get a decoding accuracy value for each set of parameters. We have 775 decoding accuracy values corresponding to the different (μ_O^*, μ_R^*) combinations for each drug preparation; Figure 4D shows decoding accuracy as a function of $|\mu_R^* - \mu_O^*|$. Although the decoding accuracies can vary for a given drug preparation, the figure convincingly shows that the no drug case generally has better decoding accuracy, consistent with our results from experiments – also, the distribution of decoding accuracies in Fig 4D are similar to Fig 1C.

We check whether our model results are consistent with the trial-to-trial variability of our data by calculating the variances of spike rate over trials, which is simply $\frac{r(1-\rho)}{\rho^2}$ for the negative binomial distribution. The values listed in Table 6 show that trial variance is consistent with the data: Mus < ND < Bic, except for retro Mus firing that has the largest variance. Recall in our data that the trends for variance of spike rate were weakest with retro stimulation with larger $p-$values (Table 4).

Table 6. Simulated trial variance of the model: $\frac{r(1-\rho)}{\rho^2} = \frac{\mu}{\rho}$.

|	Muscimol	No Drug	Bicuculline
Ortho	25.44	48.17	72.96
Retro	369.41	134.86	146.84
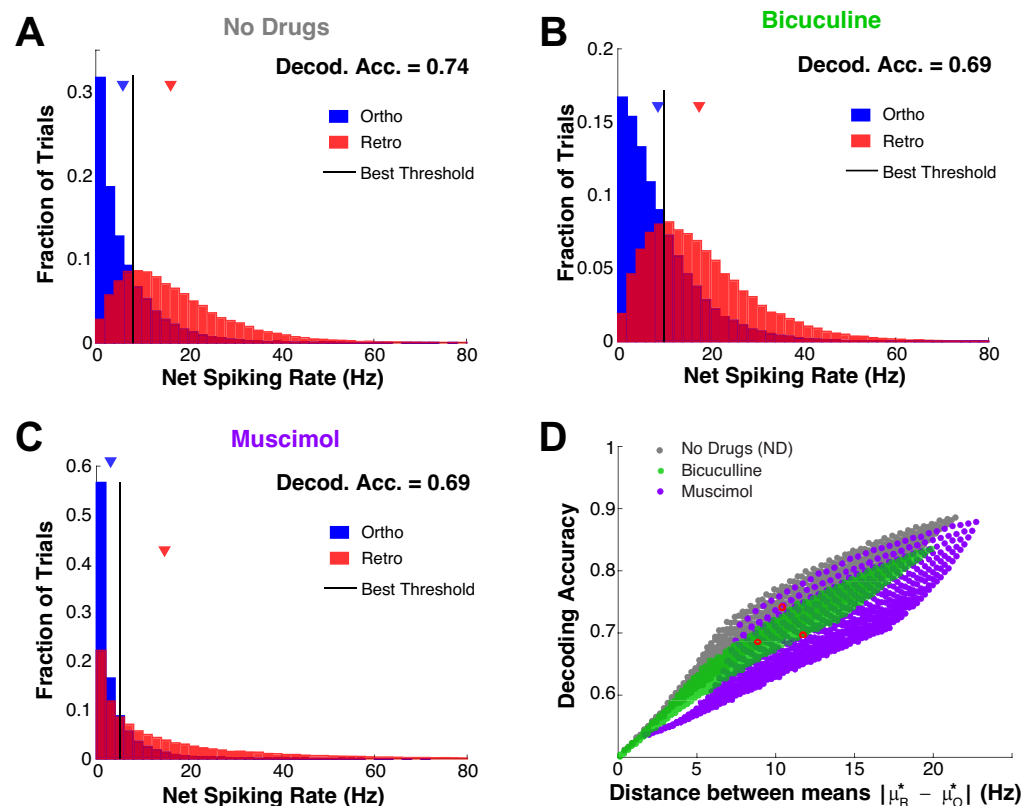
Fig 4. Model decoding accuracies with simulated trial variability. A)–C): Histograms of simulated (net) spiking rate assuming negative binomial trial-to-trial variability with the mean set to: $\frac{1}{T_{ev}} \int_0^{T_{ev}} A_E(t)\,dt$ (see Eqs (5)–(11), and solid curves in left column of Fig 3 for $A_E(t)$). **D)** Systematically varying the mean to show that the specified ρ parameter (Table 7) in negative binomial distribution generally results in no drug having best decoding accuracy (see main text for details). Red circles correspond to regimes in **A)–C)**.

Population decoding results

Thus far we have focused on decoding odor modality using the response of individual MCs. While this approach avoids making assumptions about how higher level cortical regions might use the population as a whole [13], population coding is known to be important for complicated tasks [26]. Thus, we next applied standard population coding metrics to assess how well odor modality can be decoded from populations of MCs.). We will show that modality is well-encoded, but that the differences with drug preparation are greatly diminished.

We applied two approaches to population decoding. First, we used principal component analysis (**PCA**) to project the population response onto a two-dimensional subspace of highest variance, and then applied linear discriminant analysis (**LDA**) to find an optimal decoder in that subspace (PCA+LDA). Second, we used a support vector machine (**SVM**), a common supervised learning algorithm to (nonlinearly) classify data. With both methods, we find odor modality is still encoded well above chance (Fig 5B,C). Not only is the average decoding accuracy (across recordings) higher than before (Fig 1C) but there are no longer decoding accuracies near chance level (0.5). This is perhaps expected because these metrics (PCA+LDA, SVM) exploit the higher
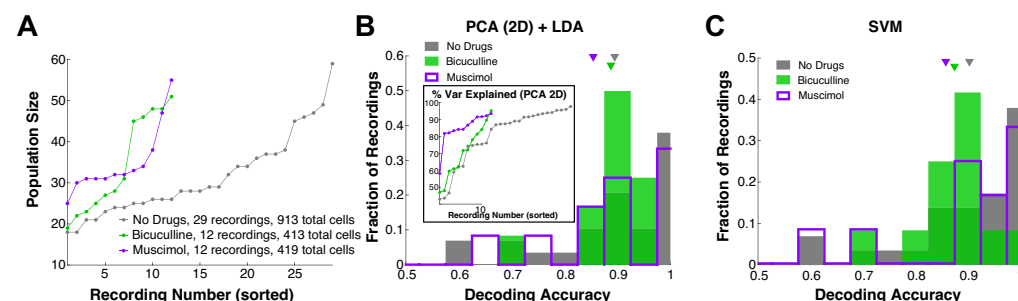
Fig 5. Population decoding of ortho versus retro is reliable and robust to altered inhibition. A) Each drug preparation has a different number of recordings and each have different number of simultaneously recorded MCs. Showing recording number and MC population size (sorted in ascending order). **B)** Decoding accuracies (one for each simultaneous recording) for all drug preparations using a 2D PCA dimension reduction following by LDA. Inset shows variance explained by PCA (sorted) by recording. **C)** Decoding accuracies using full dimensional support vector machine (**SVM**) classification. Average decoding accuracies by both methods (**B**)–**C**)) are statistically indistinguishable (minimum $p-$value for all relationships and all 3 statistical tests is: $p \geq 0.32$ for PCA+LDA, $p \geq 0.13$ for SVM).

dimensional spiking rates for a binary classification task. Note that nearly 35% of recordings with no drug and Mus have perfect decoding accuracy (Fig 5B,C).

In contrast to the case of a single MC's encoding (Fig 1C), we do not find any statistically signficant differences between the mean decoding accuracy across drug preparations. In fact, the minimum $p-$value for all relationships and all 3 statistical tests is $p \geq 0.32$ for PCA+LDA, $p \geq 0.13$ for SVM.

With these population coding metrics that amount to a binary classification problem in a high-dimensional space, the 'advantages' of the intact circuit are diminished to the point that the average decoding accuracy is no longer statistically significantly better than Bic and Mus.

Discussion

We have shown that MCs in the OB encode odor modality with our experimental data, and developed an OB model inspired by many prior studies and constrained by our rich data to analyze some of the network components of these dynamics. Despite reports that humans are able to discriminate whether food odors are delivered ortho or retronasally without being told which modality [5], it was previously unknown how this information was encoded to early cortical regions via the OB until this current study. Imaging studies of the human mouth have shown that with food odors, ortho stimuli delivery versus retro are two distinct modalities, rather than 2 different stimulus routes to the same modality, independent of odor intensity [6]. Based on *in vivo* rat data, we found significant differences in decoding accuracies (our proxy for encoding assuming an ideal observer) for classifying ortho and retronasal odors given different drug effects, but the intact (no drug) circuit had the best (average) decoding accuracy, suggesting that the OB is naturally structured to encode this important aspect of odor input.

Our model framework used prior results, data constraints [15–17], and simplicity to account for many results from our data. Prior work [1–3, 18, 19] showed differences in temporal aspects of ortho versus retro ORN inputs. We used it to investigate the circuit components that promote efficient coding of individual mitral cells with drug manipulations of inhibitory synapses. Further data analysis revealed that inhibitory

drugs have a stronger effect on the population firing with ortho stimulation than retro. 274
Using these insights, we constructed a simple firing rate model that captures the various 275
drug effects for ortho versus retro stimulus, using only a pair of E-I cells. Including 276
synaptic depression enhanced the differing drug effects. Lastly, we simulated 277
trial-to-trial variability by negative binomial random variable with mean defined by the 278
firing rate model output that captured both decoding accuracy trends and some aspects 279
of spike rate trial variability. That is, our model captures the trend that intact circuit 280
generally has better decoding accuracy than with bicuculline and muscimol, and spike 281
rate trial variance ordering: muscimol < no drug < bicuculline was apparent with ortho 282
stimulation. 283

There have been prior studied that implemented an OB circuit model with varying 284
levels of realism, but none that we are aware of that uses an OB model to account for 285
coding of odor modality and dynamics. We previously developed a realistic biophysical 286
OB network model [20] and used it to account for different neural network dynamics 287
(trial-averaged) with ortho/retro inputs, but did not focus on decoding accuracy for a 288
given trial. We note that there have been biophysical models of particular OB 289
cells [27, 28] and of the OB network [29, 30], and various models to investigate coding of 290
mixed odors [31] and learning new odors (and their concentration levels) [32], but none 291
that we know of that focus on coding of odor modality. 292

A limitation of this study is our focus on only 1 odor (EB, a food odor). We did 293
collect data from non-food odor (1-Hexanol) in our experiments, but since only food 294
odors are naturally delivered retronasally [4], we did not include 1-Hexanol in our study. 295
Moreover, it is well-known that non-food odors delivered retronasally degrade human 296
perception of odors [5, 6, 8]. Our data was collected from anesthetized rats with forced 297
air to model ortho/retro [2, 33, 34] which has clear advantages: control and a fair 298
decoding 'task' so that ortho and retro are mechanically similar with same stimulus 299
duration. In addition to the intact circuit, our data also had both increased and 300
decreased $GABA_A$ synaptic inhibition with direct manipulations in the OB. Via pooling 301
data from many rats, we had a large number MCs. Another limitation is that the rats 302
were not awake and were not eating. We are currently unaware of any data with awake 303
rodents that record MC spiking activity for the purposes of comparing ortho and retro 304
(food) odors during feeding. There are freely available MC spike data with awake 305
rodents (mice in [35, 36]) but not during feeding and not with direct manipulation of OB 306
inhibitory synapses. 307

Our results predominately center on population averages of individual MC decoding 308
accuracy because it is a logical first step [13]. Given the importance of population 309
coding for many complicated tasks [26], we also considered 2 standard population 310
decoding accuracies measures: PCA+LDA and SVM and found in both cases that the 311
intact circuit was not statistically significant better (on average). However, decoding 312
accuracy was again much higher than chance levels and better compared to average 313
individual MC decoding accuracy. Developing a heterogeneous OB model that accounts 314
for the population coding results and dynamics is daunting and beyond the scope of this 315
current study. 316

Materials and methods   317

Ethics statement   318

All procedures were carried out in accordance with the recommendations in the Guide 319
for the Care and Use of Laboratory Animals of the National Institutes of Health and 320
approved by University of Arkansas Institutional Animal Care and Use Committee 321
(protocol #14049). Isoflurane and urethane anesthesia were used and urethane overdose 322

was used for euthanasia. ₃₂₃

Code availability ₃₂₄

See `https://github.com/michellecraft64/Modality` for MATLAB code ₃₂₅
implementing the data analysis and firing rate model. ₃₂₆

Electrophysiological recordings ₃₂₇

See provided GitHub code for statistical summary of experimental data. ₃₂₈

All procedures were carried out in accordance with the recommendations in the ₃₂₉
Guide for the Care and Use of Laboratory Animals of the National Institutes of Health ₃₃₀
and approved by University of Arkansas Institutional Animal Care and Use Committee ₃₃₁
(protocol #14049). Data were collected from 11 adult male rats (240-427 g; *Rattus* ₃₃₂
Norvegicus, Sprague-Dawley outbred, Harlan Laboratories, TX, USA) housed in an ₃₃₃
environment of controlled humidity (60%) and temperature (23°C) with 12h light-dark ₃₃₄
cycles. The experiments were performed in the light phase. ₃₃₅

Surgical preparations. Anesthesia was induced with isoflurane inhalation and ₃₃₆
maintained with urethane (1.5 g/kg body weight (**bw**) dissolved in saline, ₃₃₇
intraperitoneal injection (**ip**)). Dexamethasone (2 mg/kg bw, ip) and atropine sulphate ₃₃₈
(0.4 mg/kg bw, ip) were administered before performing surgical procedures. ₃₃₉
Throughout surgery and electrophysiological recordings, core body temperature was ₃₄₀
maintained at 37°C with a thermostatically controlled heating pad. To isolate the ₃₄₁
effects of olfactory stimulation from breath-related effects, we performed a double ₃₄₂
tracheotomy surgery as described previously [2]. A Teflon tube (OD 2.1 mm, upper ₃₄₃
tracheotomy tube) was inserted 10mm into the nasopharynx through the rostral end of ₃₄₄
the tracheal cut. Another Teflon tube (OD 2.3 mm, lower tracheotomy tube) was ₃₄₅
inserted into the caudal end of the tracheal cut to allow breathing, with the breath ₃₄₆
bypassing the nasal cavity. Both tubes were fixed and sealed to the tissues using ₃₄₇
surgical thread. Local anesthetic (2% Lidocaine) was applied at all pressure points and ₃₄₈
incisions. Subsequently, a craniotomy was performed on the dorsal surface of the skull ₃₄₉
over the right olfactory bulb (2 mm × 2 mm, centered 8.5 mm rostral to bregma and ₃₅₀
1.5 mm lateral from midline). ₃₅₁

Olfactory stimulation. A Teflon tube was inserted into the right nostril was used ₃₅₂
to deliver orthonasal stimuli, and the left nostril was sealed by suturing. The upper ₃₅₃
tracheotomy tube inserted into the nasopharynx was used to deliver odor stimuli ₃₅₄
retronasally. Odorized air was delivered for 1s in duration at 1 minute intervals, with a ₃₅₅
flow rate of 250 ml/min and 1% of saturated vapor. Two odors were used: Ethyl ₃₅₆
Butyrate (**EB**, a food odor) and 1-Hexanol (**Hex**, a non-food odor). Here we limited ₃₅₇
our analysis to EB trials because food odors are perceived ortho- and retro-nasally [4]; ₃₅₈
non-food odors do not naturally occur retronasally. ₃₅₉

Electrophysiology. A 32-channel microelectrode array (MEA, A4x2tet, ₃₆₀
NeuroNexus, MI, USA) was inserted 400 μm deep from dorsal surface of OB targeting ₃₆₁
tufted and mitral cell populations. The MEA probe consisted of 4 shanks (diameter: ₃₆₂
15 μm, inter-shank spacing: 200 μm), each with eight iridium recording sites arranged in ₃₆₃
two tetrode groups near the shank tip (inter-tetrode spacing: 150 μm, within tetrode ₃₆₄
spacing 25 μm). Voltage was measured with respect to an AgCl ground pellet placed in ₃₆₅
the saline-soaked gel foams covering the exposed brain surface around the inserted ₃₆₆
MEAs. Voltages were digitized with 30 kHz sample rate (Cereplex + Cerebus, ₃₆₇
Blackrock Microsystems, UT, USA). Recordings were band-pass filtered between 300 ₃₆₈
and 3000 Hz and semiautomatic spike sorting was performed using Klustakwik software, ₃₆₉
which is well suited to the type of electrode arrays used here [37]. ₃₇₀

Data analysis

Data was collected *in vivo* from the mitral cell (**MC**) layer in the olfactory bulb (**OB**) of multiple anaesthetised rats using a multi-electrode array recording. The data consisted of spike recordings of multiple MC spike responses to Ethyl Butyrate (**EB**, a food odor) and 1-Hexanol (**Hex**, a non-food odor) presented by the two routes of stimulation, orthonasally and retronasally, for a total of 20 trials (10 ortho, 10 retro). The spike counts were calculated using 100 ms overlapping time windows over duration of a 30 s trial. However, we consider the spontaneous state to be 3 s before odor onset (defined as $t = 0$), and the evoked state to be the 1 s of odor presentation as well as 1 s of activity after odor is no longer present (i.e., 2 s total evoked state time). Further, three separate drug preparations were used in order to analyze inhibitory effects on MC spiking responses: no drug (control), Bicuculline (GABA$_A$ antagonist, i.e., decreasing inhibition), and Muscimol (GABA$_A$ agonist, i.e., increasing inhibition). See Table 1 for total number of rats and respective individual cells for each drug preparation.

Details for defining single cell decoding

We used a form of linear discriminant analysis (**LDA**) to define decoding accuracy. Decoding accuracy is defined as the fraction of trials correctly classified by a threshold that maximizes decoding accuracy. The net spiking rate $\vec{x}_k$ for the kth trial, $k = 1, 2, ..., N$, is the sum of the evoked spike counts (normalized by time window T_{ev}) minus the spikes in the spontaneous state (normalized by time window T_{sp}). Letting $s_k(t)$ be the spike train of the kth trial that is either $= 0$ (no spike) or $= \delta(t - t^*)$ (spike at t^*), we have:

$$\vec{x}_k = \frac{1}{T_{ev}} \int_0^{T_{ev}} s_k(t)\, dt - \frac{1}{T_{sp}} \int_{-T_{sp}}^0 s_k(t)\, dt \tag{4}$$

where again $t = 0$ is the time the odor is presented. There are $N = 20$ trials total (10 ortho/10 retro) for each individual cell. Then, we define multiple thresholds θ:

$$\begin{cases} \theta = x_k - \epsilon, & x_k = \max(\vec{x}_k) \\ \theta = x_k + \epsilon, & \text{else} \end{cases}$$

where an optimal threshold θ^* is determined for each individual cell as the θ that results in the most accurate separation of ortho/retro observations.

In order to more efficiently analyze the differences in decoding accuracy with different drug preparations, we selected the time windows that resulted in the most significant differences. We evaluated decoding accuracy from 100 ms to 1 s in 100 ms increments in the evoked state for each drug preparation. We then used a two sample t−test assuming unequal variances between no drug preparation and Bicuculline as well as no drug preparation and Muscimol. This resulted in 10 different p−values corresponding to each time window where the most significant p−values for both combinations of no drug/Bicuculline and no drug/Muscimol determined the optimal time window. Additionally, we repeated this process with three different lengths of time in the spontaneous state (1 s, 2 s, and 3 s) with which the evoked summed spike counts were normalized. The optimal time windows for EB odor were set to $T_{ev} = 900$ ms and $T_{sp} = 2$ s, see **S1 Fig**.

Population Decoding

The two methods are applied to each population of simultaneously recorded MCs.

PCA+LDA: For each recording, Principle Components Analysis (**PCA**) was applied to the concatenated matrix X of size $20 \times N$, where N is the number of MCs (Fig 5A),

rows 1–10 correspond to the net spiking rate with ortho and rows 11–20 correspond to retro. We only use the first two principal components and apply Linear Discriminate Analysis (**LDA**) to find a line in the 2-dimensional plane that maximizes classification accuracy [38]. We used built-in MATLAB routines `pca`, `fitcdiscr`, `predict` (see GitHub for code).

SVM: We use support vector machine with supervised 'learning' to classify data into orth or retro. We use a nonlinear classification method with Gaussian kernels, and Bayesian optimization to find the best kernel scale and box constraints for the SVM (we insured that for all recordings and drug preparations, the objective was minimized within the allowable function evaluations). After the SVM is fit to the data, the decoding accuracy is the correct classification rate obtained from the MATLAB function `kfoldLoss` using 10-fold cross-validation. We used built-in MATLAB routines (see GitHub for code).

Firing Rate (FR) model

Assuming a large population of densely coupled neurons, we use a space-clamped Wilson-Cowan rate model of coupled E-I cells: Mitral (MC, excitatory) and Periglomerular (PGC, inhibitory). The models of the respective cell firing rate, $A_j(t)$ $j \in (M, P)$, are represented by the following ordinary differential equations:

$$\tau_E \frac{dA_E}{dt} = -A_E(t) + F\Big(w_{orn,E}I_{orn}(t) - w_{EI}S_E(t)\Big) \tag{5}$$

$$\tau_I \frac{dA_I}{dt} = -A_I(t) + F\Big(w_{orn,I}I_{orn}(t) + w_{IE}S_I(t)\Big) \tag{6}$$

where the synaptic term, S_j $j \in (E, I)$, is defined by alpha-synapses with rise and decay time scales (same τ_{rise}, τ_{decay} for E/I) as follows:

$$\tau_{\text{decay}} \frac{dS_j(t)}{dt} = -S_j(t) + X_j(t) \tag{7}$$

$$\tau_{\text{rise}} \frac{dX_j(t)}{dt} = -X_j(t) + \tau_{\text{rise}}A_j(t) \tag{8}$$

In Eqs 5 and 6, $I_j(t)$ is the sum of external currents (e.g., cortical feedback, stimulus input, etc.) that varies over time to account for stimulus input, $w_{orn,j}$ are the coupling strengths of olfactory receptor neuron (**ORN**) input to j, w_{jk} are the coupling strengths from cell k to j, and the transfer function F is a threshold linear function:

$$F(x) = \max(x, 0). \tag{9}$$

Without synaptic depression, we fix $w_{IE} = 1$. With synaptic depression, we set $w_{IE}(t) = 1 + w_M(t)$, where $w_M(t)$ is governed by:

$$\tau_w \frac{dw_M}{dt} = -w_M + F_d\Big(A_E(t)\Big) \tag{10}$$

$$F_d(x) = \frac{2}{1 + e^x} - 1. \tag{11}$$

The trial-to-trial variability of net spiking rate is modeled as a negative binomial random variable:

$$\mu_{NB} = \frac{r(1 - p)}{p} \tag{12}$$

Given output from the Wilson-Cowan model $A_E(t)$, we set:

Table 7. Parameter values in firing rate model (Eqs (5)–(11)). Last 2 rows describe the parameter p in simulated trial variability using negative binomial distribution.

Parameter	Value		
τ_E	10 ms		
τ_I	5.5 ms		
τ_{decay}	10 ms		
τ_{rise}	2 ms		
τ_w	100 ms		
	Drug Preparation:		
	No Drug	**Bic**	**Mus**
w_{EI}	0.2	0.15	0.25
p for ortho	0.12	0.12	0.12
p for retro	0.12	0.12	0.04

$$\mu_{NB} = \frac{1}{T_{ev}} \int_0^{T_{ev}} A_E(t)dt \tag{13}$$

by manually determining the p parameter in the negative binomial distribution (see Table 7) for each drug preparation, and setting the parameter $r = \mu_{NB}p/(1-p)$.

Supporting information

S1 Fig. Varying windows for spike count. Net spike counts in a given trial were total spike counts in evoked window minus total spike counts in spontaneous window. Vertical axes show p−values (log-scale) from comparisons of average decoding accuracies with different drug preparations using two different statistical tests: two sample t−test assuming unequal variance (**A**) and Wilcoxon rank sum test (**B**). Open circles compares no drug to Bic, closed circles compare no drug to Mus, and colors denote different spontaneous time windows (see legend). **C), D)** are similar to **A),B)** except the first 300 ms of the evoked state are removed to test whether decoding accuracies increase and are significant (they were not); this was based on the population PSTH being similar for ortho and retro immediately after stimulus onset (Fig 1Aii). Decoding accuracies are significantly different ($\alpha = 0.01$, denoted by dashed black line) for a large range of spontaneous and evoked windows; we chose 2 s for spontaneous and 0.9 s for evoked (keeping the entire time, not excluding the first 300 ms) because they largely gave the smallest p−values. All with EB (food odor).

S2 File. Detailing 'Decoding accuracy dynamics from drug effects on population-averaged firing rates.'

S3 Fig. Decoding accuracy dynamics from drug effects on population-averaged firing rates.

Author Contributions

MC programmed and implemented the software, including the data analysis. MC and CL developed the computational models. MC, AKB, WLS, CL conceptualized and developed the project. SHG and WLS designed the experiments and collected the data.

MC and CL drafted the original manuscript. MC, AKB, SHG, WLS, CL edited the manuscript. MC and CL developed the visualizations. CL supervised the project. 467 468

References 469

1. Sanganahalli BG, Baker KL, Thompson GJ, Herman P, Shepherd GM, Verhagen JV, et al. Orthonasal versus retronasal glomerular activity in rat olfactory bulb by fMRI. NeuroImage. 2020;212. 470 471 472

2. Gautam SH, Verhagen JV. Retronasal odor representations in the dorsal olfactory bulb of rats. The Journal of Neuroscience. 2012;32(23):7949–7959. 473 474

3. Furudono Y, Cruz G, Lowe G. Glomerular input patterns in the mouse olfactory bulb evoked by retronasal odor stimuli. BMC neuroscience. 2013;14(1):45. 475 476

4. Small DM, Gerber JC, Mak YE, Hummel T. Differential neural responses evoked by orthonasal versus retronasal odorant perception in humans. Neuron. 2005;47(4):593–605. doi:10.1016/j.neuron.2005.07.022. 477 478 479

5. Frasnelli J, Ungermann M, Hummel T. Ortho-and retronasal presentation of olfactory stimuli modulates odor percepts. Chemosensory Perception. 2008;1(1):9–15. 480 481 482

6. Bender G, Hummel T, Negoias S, Small DM. Separate signals for orthonasal vs. retronasal perception of food but not nonfood odors. Behavioral neuroscience. 2009;123(3):481. 483 484 485

7. Blankenship ML, Grigorova M, Katz DB, Maier JX. Retronasal odor perception requires taste cortex, but orthonasal does not. Current biology. 2019;29(1):62–69. 486 487

8. Hannum ME, Fryer JA, Simons CT. Non-food odors and the Duality of Smell: Impact of odorant delivery pathway and labeling convention on olfactory perception. Physiology & Behavior. 2021;238:113480. 488 489 490

9. Mandairon N, Linster C. Odor perception and olfactory bulb plasticity in adult mammals. Journal of neurophysiology. 2009;101(5):2204–2209. 491 492

10. Wilson RI, Laurent G. Role of GABAergic inhibition in shaping odor-evoked spatiotemporal patterns in the Drosophila antennal lobe. Journal of Neuroscience. 2005;25(40):9069–9079. 493 494 495

11. Tan J, Savigner A, Ma M, Luo M. Odor information processing by the olfactory bulb analyzed in gene-targeted mice. Neuron. 2010;65(6):912–926. 496 497

12. Abraham NM, Egger V, Shimshek DR, Renden R, Fukunaga I, Sprengel R, et al. Synaptic inhibition in the olfactory bulb accelerates odor discrimination in mice. Neuron. 2010;65(3):399–411. 498 499 500

13. Rolls ET, Treves A. The neuronal encoding of information in the brain. Progress in neurobiology. 2011;95(3):448–490. 501 502

14. Churchland MM, Yu BM, et al. Stimulus onset quenches neural variability: a widespread cortical phenomenon. Nature Neuroscience. 2010;13:369–378. 503 504

15. Xiao ZC, Lin KK, Young LS. A data-informed mean-field approach to mapping of cortical parameter landscapes. PLoS computational biology. 2021;17(12):e1009718. 505 506 507

16. Ly C, Barreiro AK, Gautam SH, Shew WL. Odor-evoked increases in olfactory bulb mitral cell spiking variability. iScience. 2021;24(9):102946.

17. Barreiro A, Gautam SH, Shew W, Ly C. A theoretical framework for analyzing coupled neuronal networks: Application to the olfactory system. PLoS Computational Biology. 2017;13:e1005780. doi:10.1371/journal.pcbi.1005780.

18. Scott JW, Acevedo HP, Sherrill L, Phan M. Responses of the rat olfactory epithelium to retronasal air flow. Journal of neurophysiology. 2007;97(3):1941–1950.

19. Carey RM, Verhagen JV, Wesson DW, Pírez N, Wachowiak M. Temporal structure of receptor neuron input to the olfactory bulb imaged in behaving rats. Journal of neurophysiology. 2009;101(2):1073–1088.

20. Craft MF, Barreiro A, Gautam SH, Shew WL, Ly C. Differences in olfactory bulb mitral cell spiking with ortho- and retronasal stimulation revealed by data-driven models. PLoS Computational Biology. 2021;17(9):e1009169. doi:10.1371/journal.pcbi.1009169.

21. Rall W, Shepherd GM, Reese TS, Brightman MW. Dendrodendritic synaptic pathway for inhibition in the olfactory bulb. Experimental neurology. 1966;14(1):44–56.

22. Cang J, Isaacson JS. In vivo whole-cell recording of odor-evoked synaptic transmission in the rat olfactory bulb. Journal of Neuroscience. 2003;23(10):4108–4116.

23. Jordan R, Fukunaga I, Kollo M, Schaefer AT. Active sampling state dynamically enhances olfactory bulb odor representation. Neuron. 2018;98(6):1214–1228.

24. Wang ZJ, Sun L, Heinbockel T. Cannabinoid receptor-mediated regulation of neuronal activity and signaling in glomeruli of the main olfactory bulb. Journal of Neuroscience. 2012;32(25):8475–8479.

25. Dietz SB, Murthy VN. Contrasting short-term plasticity at two sides of the mitral–granule reciprocal synapse in the mammalian olfactory bulb. The Journal of physiology. 2005;569(2):475–488.

26. Saxena S, Cunningham JP. Towards the neural population doctrine. Current opinion in neurobiology. 2019;55:103–111.

27. Viertel R, Borisyuk A. A Computational model of the mammalian external tufted cell. Journal of theoretical biology. 2019;462:109–121.

28. Li G, Cleland TA. A two-layer biophysical model of cholinergic neuromodulation in olfactory bulb. Journal of Neuroscience. 2013;33(7):3037–3058.

29. Bathellier B, Lagier S, Faure P, Lledo PM. Circuit properties generating gamma oscillations in a network model of the olfactory bulb. Journal of neurophysiology. 2006;95(4):2678–2691.

30. Li G, Cleland TA. A coupled-oscillator model of olfactory bulb gamma oscillations. PLoS computational biology. 2017;13(11):e1005760.

31. Grabska-Barwińska A, Barthelmé S, Beck J, Mainen ZF, Pouget A, Latham PE. A probabilistic approach to demixing odors. Nature Neuroscience. 2017;20:98–106.

32. Hiratani N, Latham PE. Rapid Bayesian learning in the mammalian olfactory system. Nature communications. 2020;11(1):3845. 550 551

33. Gautam SH, Verhagen JV. Direct behavioral evidence for retronasal olfaction in rats. PloS one. 2012;7(9):e44781. 552 553

34. Gautam SH, Short SM, Verhagen JV. Retronasal odor concentration coding in glomeruli of the rat olfactory bulb. Frontiers in Integrative Neuroscience. 2014;8:81–81. 554 555 556

35. Bolding KA, Franks KM. Recurrent cortical circuits implement concentration-invariant odor coding. Science. 2018;361(6407). 557 558

36. Bolding K, Franks K. Simultaneous extracellular recordings from mice olfactory bulb (OB) and piriform cortex (PCx) and respiration data in response to odor stimuli and optogenetic stimulation of OB. CRCNS org Date accessed: January. 2021;. 559 560 561 562

37. Rossant C, Kadir S, Goodman D, Schulman J, Hunter M, Saleem A, et al. Spike sorting for large, dense electrode arrays. Nature neuroscience. 2016;19(4):634–641. 563 564

38. Cunningham JP, Yu BM. Dimensionality reduction for large-scale neural recordings. Nature neuroscience. 2014;17(11):1500–1509. 565 566